

High-Frequency Prior-Driven Adaptive Masking for Accelerating Image Super-Resolution

Wei Shang^{1,2}, Dongwei Ren³, Wanying Zhang¹, Pengfei Zhu³, Qinghua Hu³, Wangmeng Zuo¹

¹School of Computer Science and Technology, Harbin Institute of Technology

²City University of Hong Kong ³Tianjin University

Abstract

The primary challenge in accelerating image super-resolution lies in reducing computation while maintaining performance and adaptability. Motivated by the observation that high-frequency regions (e.g., edges and textures) are most critical for reconstruction, we propose a training-free adaptive masking module for acceleration that dynamically focuses computation on these challenging areas. Specifically, our method first extracts high-frequency components via Gaussian blur subtraction and adaptively generates binary masks using K-means clustering to identify regions requiring intensive processing. Our method can be easily integrated with both CNNs and Transformers. For CNN-based architectures, we replace standard 3×3 convolutions with an unfold operation followed by 1×1 convolutions, enabling pixel-wise sparse computation guided by the mask. For Transformer-based models, we partition the mask into non-overlapping windows and selectively process tokens based on their average values. During inference, unnecessary pixels or windows are pruned, significantly reducing computation. Moreover, our method supports dilation-based mask adjustment to control the processing scope without retraining, and is robust to unseen degradations (e.g., noise, compression). Extensive experiments on benchmarks demonstrate that our method reduces FLOPs by 24–43% for state-of-the-art models (e.g., CARN, SwinIR) while achieving comparable or better quantitative metrics. The source code is available at <https://github.com/shangwei5/AMSR>.

1. Introduction

The primary goal of super-resolution (SR) is to enhance image resolution through the generation of finer structural details that accurately reconstruct high-frequency components in the original scene. This technique addresses critical requirements in applications demanding high-resolution (HR) images from limited sources, such as satellite imaging [23],

medical imaging [24], and surveillance [37].

The evolution of deep learning has driven a proliferation of convolutional neural network (CNN)-based architectures for single image super-resolution (SISR). While achieving superior performance, deeper networks unavoidably incur significant (floating-point operations) FLOPs overhead, thereby driving recent research to focus on lightweight model design [2, 7, 17, 30, 36] and intelligent computation allocation strategies [3, 9, 12, 26]. The latter achieves efficiency optimization by adaptively allocating computational resources according to the local reconstruction complexity, thereby reducing computational operations while maintaining reconstruction quality. These approaches can be seamlessly integrated into conventional CNN-based networks.

Current adaptive SR methods can be categorized into two classes: patch-distributing approaches [3, 12, 26] and pixel-distributing approach [9]. Existing patch-based implementations partition images into sub-regions for difficulty assessment and differentiated processing. However, these methods suffer from an inherent limitation: intra-patch heterogeneity may lead to suboptimal resource allocation, as uniform processing is applied to mixed-complexity regions. Pixel-distributing methods [9] address this issue by providing fine-grained partitioning of regions according to the degree of restoration difficulty. However, its computational advantages are restricted to the upsampling stages in contemporary deep architectures. Moreover, most existing implementations depend on auxiliary classifiers for region partitioning, introducing additional training complexity.

To address the aforementioned issues, we present an efficient acceleration framework that maintains end-to-end training while significantly reducing inference complexity. Our method builds upon two key innovations: frequency-aware region decomposition and architecture-agnostic computation pruning. Existing analysis reveals that the classification of restoration difficulty in [3, 9, 12] exhibit strong correlations with image high-frequency components. This observation motivates our training-free adaptive masking module, which employs Gaussian blur subtraction followed by K-means binarization to generate adaptive processing

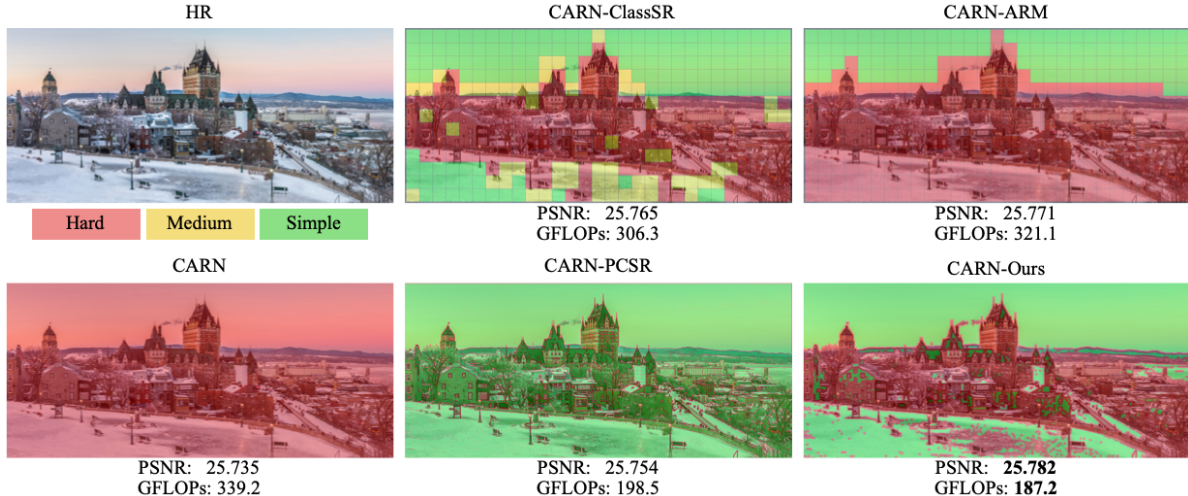


Figure 1. Visualization of the $\times 4$ SR results of the image “1400” from Test4K. Compared to other methods, our method employs high-frequency information to adaptively identify regions requiring network processing at the pixel level, thereby achieving comparable PSNR performance while significantly reducing computation. Masks of different colors indicate the varying levels of complexity with which different methods process distinct regions of the image.

masks (Fig. 1), eliminating the need for classifiers.

The proposed acceleration strategy demonstrates remarkable architectural compatibility. For CNN-based frameworks, since 3×3 convolutions constitute the majority of the network, we implement parameter-preserving transformations through: 1) feature unfolding with 3×3 kernels to maintain receptive fields, 2) strategic replacement of standard 3×3 convolutions with expanded-channel 1×1 convolutions ($9 \times$ channel increase compensating for kernel reduction). For Transformer-based architectures, we partition the mask into windows and calculate their mean values, which are then compared against the pruning threshold to guide token-level processing decisions. Crucially, our implementation preserves full computational graphs during training through zero-masking of pruned elements, while enabling dynamic computation skipping during inference through pixels or tokens pruning to reduce computation.

In summary, our method achieves three fundamental advancements: 1) training-free adaptive masking for complexity reduction, 2) architecture-independent computation allocation via frequency-driven masks, and 3) simplified end-to-end training without extra auxiliary supervision. We have outlined the advantages of our approach compared to other methods in Table 1. Comprehensive experiments confirm the effectiveness of our method, and a distinct advantage in terms of speed compared to other acceleration techniques.

2. Related Work

2.1. Region-Irrelevant SISR

Dong *et al.* [6] are the pioneers in employing CNNs to address the challenge of SISR, achieving substantial suc-

Characteristics	ClassSR [12]	ARM [3]	APE [26]	PCSR [9]	Ours
w/o classifiers?	✗	✓	✗	✗	✓
w/o post-processing?	✗	✗	✗	✗	✓
Pixel-distributing?	✗	✗	✗	✓	✓
Single-stage training?	✗	✓	✓	✗	✓

Table 1. Characteristic comparison over prior works.

cess. Since their groundbreaking work, a large number of deep learning-based SR algorithms have been proposed [7, 18, 19, 33, 34]. Kim *et al.* [10] proposed a deeper neural network to achieve superior results and improved convergence speed by learning image residuals. SRResNet [13] enhanced the network architecture by incorporating residual blocks to further boost the performance. Building on this foundation, EDSR [19] streamlined the structure by eliminating some unnecessary components, thereby achieving an improved performance once again. Zhang *et al.* [33, 34] adopted dense connections and the attention mechanism to design deeper networks to refresh the state-of-the-art. With the advancement of Vision Transformers, their strong capabilities have also been harnessed in the domain of SISR [4, 5, 18], leading to improved performance. However, as networks have evolved, there has been a corresponding increase in the number of network parameters and computation.

To mitigate the computational burden, numerous researchers have dedicated their efforts to the development of lightweight SR. FSRCNN [7] first proposed to work on LR images for accelerating SR. CARN [2] adopted group convolutions to design a cascading residual network for fast

processing. PAN [36] applied pixel attention for enhancing details within an effective network. Additionally, some researchers have combined special strategies to achieve a lightweight model. For instance, [14] and [31] proposed utilizing Neural Architecture Search (NAS) to optimize network structures and employing parameter pruning to reduce the model size. [16, 20, 29] are indicative of the trend towards representing full-precision SISR models with a lower-bit format. Knowledge distillation is often regarded as an effective way to enhance the quality of reconstructed images from lightweight models [15, 35]. Overall, these methods lack input-adaptive computation allocation, enforcing uniform processing across all spatial regions regardless of local restoration complexity.

2.2. Region-Aware SISR

Recently, some researchers discovered that high-frequency regions are often more challenging to restore than low-frequency regions [3, 25, 28], prompting adaptive computation reduction strategies. AdaDSR [21] utilized a lightweight adapter module to predict the network depth map to optimize efficiency. SMSR [25] introduces sparse masks upon spaces and channels within each block to prune redundant computation. FAD [28] used multiple convolutional branches of different sizes and different regions were fed to branches according to the frequency of this region. ClassSR [12] trained a classifier to categorize image patches into three types according to the patch difficulty and assigned them to backbone networks with different widths to reduce FLOPs. APE [26] utilized a regressor to predict the incremental capacity of each layer for each patch, reducing FLOPs by early exiting. ARM [3] adopted a supernet containing many subnets of different sizes to deal with image patches according to an Edge-to-PSNR lookup table. PCSR [9] incorporated a pixel-level classifier following the feature extraction module in the backbone network. Depending on the classification outcome, pixels from distinct regions are directed into different upsamplers with different widths. In contrast to the aforementioned method, we obtain the training-free mask based on high-frequency priors bypass learned classifiers. Our approach reduces computation without introducing additional parameters or modules. Unified mask propagation mechanisms ensure compatibility with both CNNs and Transformers.

3. Proposed Method

3.1. Preliminary

Given an LR image x , where $x \in \mathbb{R}^{H \times W \times 3}$, and H and W are the image height and width, respectively, the goal of $\times \alpha$ SR is to reconstruct an HR image \hat{y} with $\hat{y} \in \mathbb{R}^{(\alpha H) \times (\alpha W) \times 3}$. The architecture of most SR methods is commonly structured into three main components: head,

body, and tail. The head part initiates the process by encoding the input image into features f with $f \in \mathbb{R}^{H \times W \times C}$, and C is the channel number of the features:

$$f = \text{Head}(x), \quad (1)$$

where $\text{Head}(\cdot)$ is commonly achieved through a singular convolution layer.

Subsequently, these features are fed into the body part to further extract deep features d with $d \in \mathbb{R}^{H \times W \times C}$:

$$d = \text{Body}(f). \quad (2)$$

For the majority of SR networks, $\text{Body}(\cdot)$ accounts for the bulk of the total parameters, hence, most methodologies [2, 7, 13, 18] primarily focus on designing this part.

Finally, the tail part converts the deep features into a high-resolution output image \hat{y} with $\hat{y} \in \mathbb{R}^{(\alpha H) \times (\alpha W) \times 3}$:

$$\hat{y} = \text{Tail}(d). \quad (3)$$

Typically, $\text{Tail}(\cdot)$ is composed of upsampling operations (e.g., interpolation, pixel shuffle, or transposed convolutions) and convolution layers.

The motivation of our method is based on two critical observations. First, computational allocation within network architectures demonstrates progressive migration toward the body part as the performance of models increases. For instance, it accounts for 3% in FSRCNN [7], 58% in CARN [2], and 99% in SwinIR [18]. This progression motivates our accelerating strategy: rather than modifying head and tail components, we precisely modulate computation through selective identification of feature-rich regions requiring intensive extraction. Second, we strategically avoid post-processing operations, which are typically employed to rectify artifacts due to the use of different upsamplers in the tail part [9]. Our framework instead focuses computational resources on the body part while maintaining the tail as a trainable refinement module. Furthermore, our operation does not rely on patch-level processing, thus eliminating the need for patch classification and pre-segmentation as required in [3, 12, 26], which ensures good efficiency.

3.2. High-Frequency Mask Generation

To implement the selection of specific pixels for processing, we require an efficient scheme for mask generation. Building upon previous methods that have identified challenging regions in images as those with a rich presence of high-frequency information, we draw inspiration from [30], which adopted a straightforward and effective approach to extract high-frequency information from the LR images. Specifically, we apply a Gaussian blur operation to the LR image to generate its blurred counterpart, which serves as an image containing uniform signals. Subsequently, we subtract this blurred image from the original LR input to extract

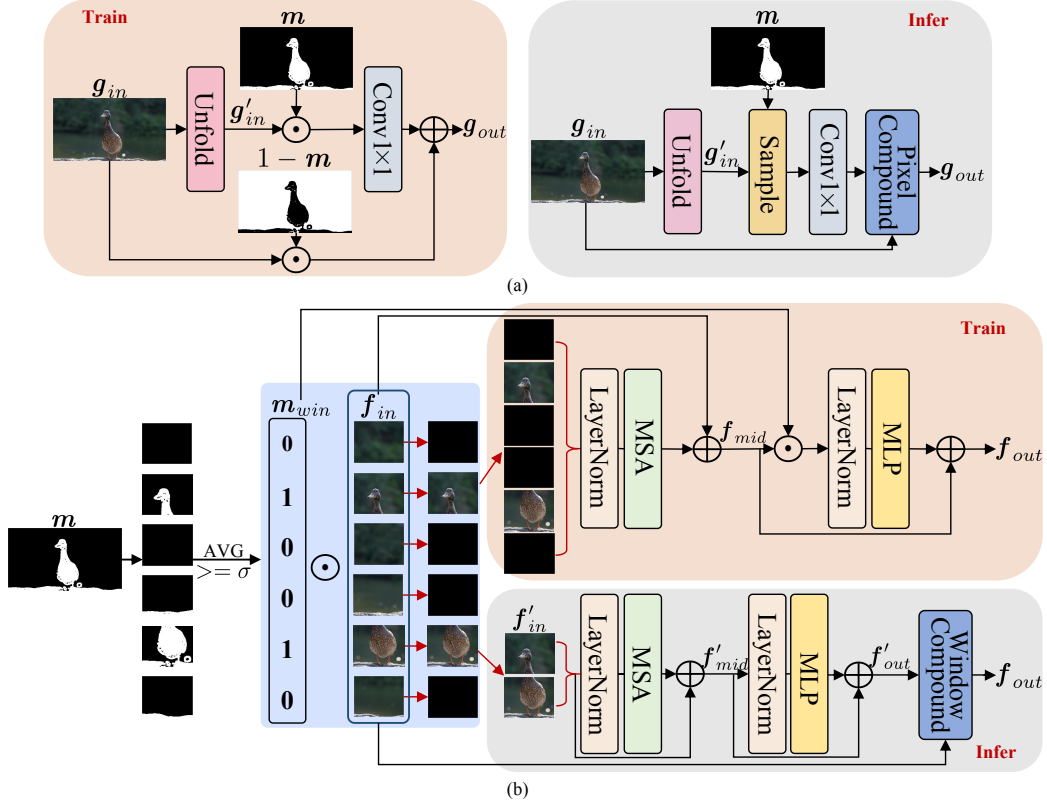


Figure 2. Overview of key differences in various architectures. (a) For CNN-based methods, we utilize the unfold operation to expand features to achieve a receptive field equivalent to that of a 3×3 convolution, facilitating subsequent spatially invariant 1×1 convolution operations. During training, to ensure backward propagation, we apply m to exclude regions that do not require processing. In the testing phase, we sample pixels that require processing based on m , thereby reducing computation. (b) We compute pruning decisions m_{win} based on the mask corresponding to each token. During training, all tokens are fed into the module, while during testing, only the necessary tokens are retained to complete acceleration. The terms "AVG" and " σ " refer to the average pooling operation and the threshold of the average pooling operation, respectively.

the high-frequency components. We set the blur kernel size to 5, and the standard deviation to 1 following [30].

In light of findings from prior research, [3] has established that some flat regions benefit more from direct interpolation, and [9] has indicated that more sophisticated classification for various regions contributes marginally to performance gains. Consequently, we binarize the high-frequency map to obtain high-frequency mask m , to selectively process only the regions requiring extensive feature extraction by the body part of the network, leaving the remaining regions unprocessed. Specifically, we utilize the K-means clustering to categorize the values within the high-frequency map into two groups, initializing the cluster centers at 0.5, framing as an adaptive selection. A comparative analysis of adaptive selection against fixed thresholding is presented in Sec. 4.4.1. Moreover, our adaptive selection of the high-frequency map demonstrates greater robustness compared to classifier-based selection (please refer to Sec. 4.3). Additionally, our mask generation is training-

free, and the clustering requires only a few iterations to converge, typically less than 10, rendering it highly efficient (please refer to Table 3). We can apply a dilation operation to the mask to achieve better scalability (please refer to ref 4.4.2).

3.3. Main Changes of Architecture

3.3.1. CNN-based Network

For CNN-based methods, to accommodate spatial sparsity within our operations, we substitute the prevalent 3×3 convolutional layers in the body part of the network with 1×1 convolutions, as shown in Fig. 2 (a). This substitution is executed with stringent adherence to two facets of consistency: the equivalence of computation and parameters, alongside the preservation of the receptive field. To this end, we initially apply an unfold operation with the kernel size of 3 to the input features $g_{in} \in \mathbb{R}^{H \times W \times C}$, which expands them into features $g'_{in} \in \mathbb{R}^{H \times W \times (C \times 3 \times 3)}$ that maintains the same receptive field as the 3×3 convolution operation.

Methods	Params	Test2K		Test4K		Test8K	
		PSNR	GFLOPs	PSNR	GFLOPs	PSNR	GFLOPs
FSRCNN	25K	25.650	45.3 (100%)	<u>26.952</u>	185.3 (100%)	32.696	1067.8 (100%)
FSRCNN-ClassSR	113K	25.619	38.4 (84.8%)	26.918	146.1 (78.8%)	32.732	707.6 (66.3%)
FSRCNN-ARM	25K	25.644	35.5 (78.4%)	26.934	134.9 (72.8%)	32.750	664.9 (62.3%)
FSRCNN-PCSR	25K	<u>25.661</u>	17.1 (37.7%)	26.947	79.4 (42.8%)	<u>32.768</u>	509.1 (47.7%)
FSRCNN-Ours	22K	25.663	38.6 (85.2%)	26.955	157.5 (85.0%)	32.772	904.4 (84.7%)
CARN	295K	26.022	112.0 (100%)	27.405	457.8 (100%)	33.141	2638.6 (100%)
CARN-ClassSR	645K	26.020	100.3 (89.6%)	<u>27.430</u>	378.5 (82.7%)	33.252	1800.1 (68.2%)
CARN-ARM	295K	<u>26.029</u>	84.3 (75.3%)	<u>27.430</u>	328.8 (71.8%)	33.279	1738.8 (65.9%)
CARN-PCSR	169K	26.023	68.7 (61.3%)	27.429	277.7 (60.7%)	<u>33.283</u>	1646.3 (62.4%)
CARN-Ours	196K	26.034	64.7 (57.8%)	27.433	256.1 (55.9%)	33.284	1393.9 (52.8%)
SRResNet	1.5M	26.223	502.9 (100%)	27.657	2056.2 (100%)	33.416	11850.7 (100%)
SRResNet-ClassSR	3.1M	26.212	445.2 (88.5%)	27.663	1683.9 (81.9%)	33.508	7981.5 (67.4%)
SRResNet-ARM	1.5M	26.215	394.8 (78.5%)	<u>27.669</u>	1502.2 (73.1%)	33.520	7398.9 (62.4%)
SRResNet-PCSR	1.1M	<u>26.216</u>	388.2 (77.2%)	27.662	1486.6 (72.3%)	<u>33.528</u>	7352.0 (62.0%)
SRResNet-Ours	1.2M	26.223	349.6 (69.5%)	27.670	1367.3 (66.5%)	33.532	7287.8 (61.5%)
SwinIR	930K	<u>26.323</u>	102.6 (100%)	<u>27.802</u>	415.0 (100%)	<u>33.651</u>	2399.8 (100%)
SwinIR-Ours	930K	26.347	78.4 (76.4%)	27.811	289.9 (69.9%)	33.666	1411.5 (58.8%)

Table 2. The comparison of the previous methods and our method on the large image SR benchmarks: Test2K, Test4K, and Test8K with $\times 4$ SR. **Bold** and underline are used to indicate top 1st and 2nd, respectively.

Concurrently, we amplify the input channel for the 1×1 convolution by a factor of 9, ensuring the consistency of parameters and computation.

During training, to ensure backward propagation of gradients at all pixels, we perform element-wise multiplication between the output features and the mask \mathbf{m} to exclude the pixels that are to be pruned, and finally combine these with the input features to form the final output features $\mathbf{g}_{out} \in \mathbb{R}^{H \times W \times C}$:

$$\mathbf{g}_{out} = \text{Conv}(\mathbf{g}'_{in} \odot \mathbf{m}) + \mathbf{g}_{in} \odot (\mathbf{1} - \mathbf{m}). \quad (4)$$

In the testing phase, by sampling the unfolded features and selecting the regions that require processing before passing them through the 1×1 convolutions, while leaving unprocessed the remaining areas. Lastly, the processed regions are placed back into the original feature map according to the mask to obtain the final output features \mathbf{g}_{out} . It is not difficult to calculate the computation of this operation: $Q \times C \times (9 \times C)$, $Q \ll H \times W$, where Q is the number of sampled pixels. Compared to the original computation $H \times W \times C \times C \times 9$, our operation accounts for only a small fraction $\frac{Q}{H \times W}$.

3.3.2. Transformer-based Network

Distinguished from CNN-based methods, Transformer-based methods focus on feature extraction at the token level. To avoid incurring substantial computation, they partition the input into non-overlapping windows for processing. We employ SwinIR [18] as an example to illustrate our token pruning strategy. We consider each window patch in SwinIR as a token. Specifically, we partition the mask \mathbf{m} into windows, and then compares the average value of each window to the threshold σ . We obtain the pruning decision

Backbone	Method	Test2K	Test4K	Test8K
FSRCNN	+ClassSR	161ms	773ms	4536ms
	+ARM	104ms	528ms	3280ms
	+PCSR	84ms	211ms	991ms
	+Ours	6ms	16ms	69ms
CARN	+ClassSR	723ms	3605ms	20.99s
	+ARM	703ms	3214ms	19.68s
	+PCSR	90ms	274ms	1.49s
	+Ours	74ms	224ms	1.22s
SRResNet	+ClassSR	545ms	2754ms	15.86s
	+ARM	508ms	2378ms	15.11s
	+PCSR	153ms	543ms	2.99s
	+Ours	100ms	349ms	1.73s

Table 3. Comparison of running time per image on $\times 4$ SR.

\mathbf{m}_{win} , where tokens with average values below this threshold will be set as 0, otherwise they will be set as 1.

During the training process, to ensure that batch training can be conducted effectively, all tokens, including those that have been pruned, are fed into the Swin Transformer Layer (STL) together, STL contains LayerNorm (LN), multi-layer perceptron (MLP) and multi-head self-attention (MSA) as shown in Fig. 2 (b). This process can be represented as follows:

$$\begin{aligned} \mathbf{f}_{mid} &= \text{MSA}(\text{LN}(\mathbf{f}_{in} \odot \mathbf{m}_{win})) + \mathbf{f}_{in}, \\ \mathbf{f}_{out} &= \text{MLP}(\text{LN}(\mathbf{f}_{mid} \odot \mathbf{m}_{win})) + \mathbf{f}_{mid}. \end{aligned} \quad (5)$$

During the testing process, we can significantly reduce the computation by directly pruning tokens that do not require processing, based on the pruning decision \mathbf{m}_{win} . This

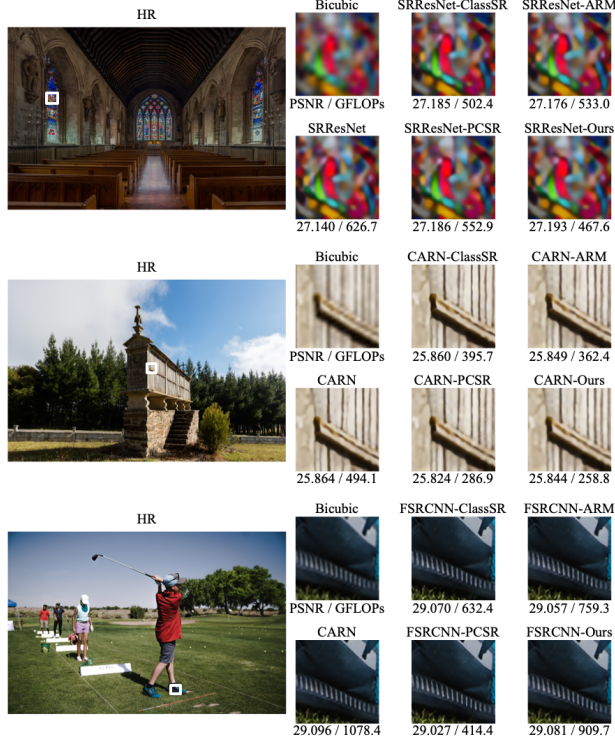


Figure 3. Visual comparison of our methods with backbone networks, and SOTA dynamic SISR method with $\times 4$ super-resolution. These examples are image “1258” (above) from Test2K, image “1399” (middle) from Test4K, and image “1405” (below) from Test8K respectively. Our method achieves comparable performance and lower computation except for FSRCNN.

process can be represented as follows:

$$\begin{aligned} \mathbf{f}'_{in} &= \text{PR}(\mathbf{f}_{in}, \mathbf{m}_{win}), \\ \mathbf{f}'_{mid} &= \text{MSA}(\text{LN}(\mathbf{f}'_{in})) + \mathbf{f}'_{in}, \\ \mathbf{f}'_{out} &= \text{MLP}(\text{LN}(\mathbf{f}'_{mid})) + \mathbf{f}'_{mid}, \end{aligned} \quad (6)$$

where $\text{PR}(\cdot)$ is a token pruning operation. Tokens with a value of 0 in the pruning decision \mathbf{m}_{win} are pruned. Finally, we place processed tokens \mathbf{f}'_{out} back to their original locations to replace the corresponding tokens in \mathbf{f}_{in} , obtaining the output feature \mathbf{f}_{out} .

4. Experiments

4.1. Settings

4.1.1. Datasets

All models are trained on DIV2K [1], which comprises 800 high-resolution images. Following the training setting in [3, 9, 12], we partition these images into 1.59 million 32×32 LR sub-images for training. Random rotation and flipping are applied for data augmentation. For the testing dataset, we select 300 images (index 1201 – 1500) from

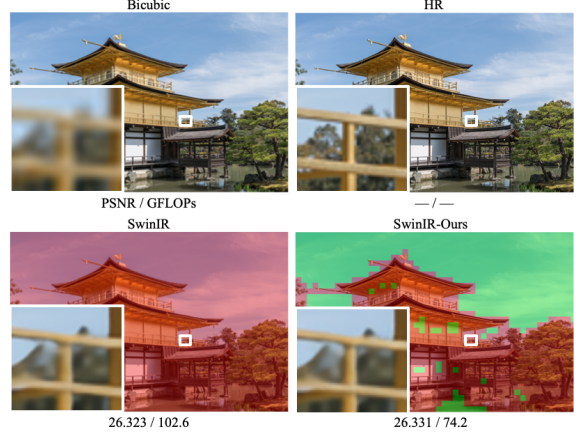


Figure 4. Visual comparison of our method with the backbone network. These examples are image “1300” from Test2K.

	Test2K		Test4K		Test8K	
	PSNR	GFLOPs	PSNR	GFLOPs	PSNR	GFLOPs
1)	25.552	60.07	26.791	237.2	32.593	1299.2
2)	25.550	61.58	26.814	251.4	32.601	1445.8
3)	25.927	61.83	27.307	244.5	33.162	1335.8

Table 4. The effects of different strategies for generating high-frequency masks.

DIV8K [8]. Following [3, 9, 12], we divide these three hundred images evenly into three groups. The first two groups are downsampled to 2K and 4K resolution, respectively, to serve as HR images of Test2K and Test4K. The third group is used directly as HR images of Test8K. The LR images are obtained following the previous work [12].

4.1.2. Implementation Details

To ensure generality and comprehensiveness, we have selected backbones based on both CNNs and Transformers. We adopt FSRCNN [7], CARN [2], and SRResNet [13] for CNN-based backbones and SwinIR [18] for the transformer-based backbone. The batch size is set as 64 for FSRCNN and 16 for CARN, SRResNet, and SwinIR. The initial learning rate is set as 1×10^{-3} for FSRCNN and 2×10^{-4} for CARN, SRResNet, and SwinIR with cosine annealing scheduling [22]. \mathcal{L}_1 loss [27] is adopted with Adam optimizer [11] and all models are trained with 2,000K iterations. To ensure the stability of the training process, we initially set the mask as 1. We then apply the dilation operation with a large kernel size to the high-frequency mask and gradually reduce the kernel size over the course of training to incrementally discard a greater number of pixels/tokens, thereby achieving a stable training process. During testing, we set the dilation kernel size to 5 for FSRCNN and CARN, 7 for SRResNet, and 11 for SwinIR. And the pruning threshold σ is set to 0.5 for SwinIR.

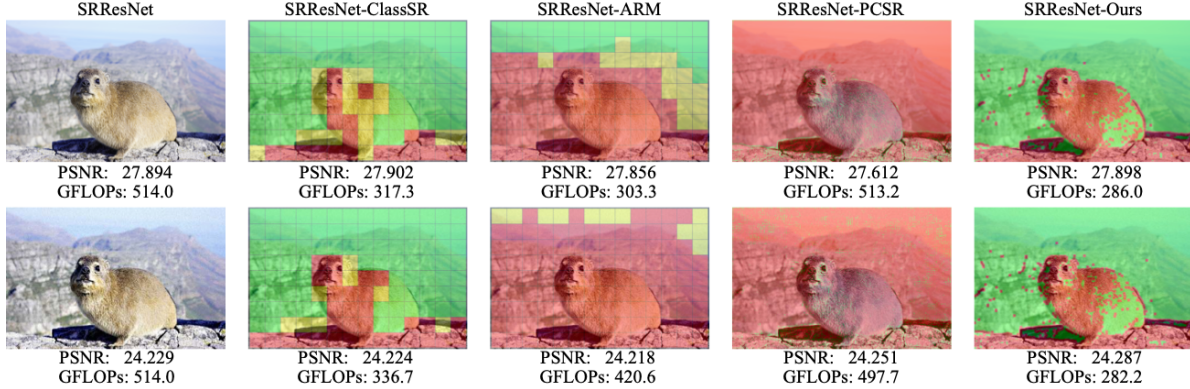


Figure 5. Illustration of the $\times 4$ SR results of the image "1244" from Test2K under different degradations. The first row presents the results when the degradations are aligned with those used during training [12]. The second row displays the results employing a more extensive and complex set of random degradations [32].

4.2. Comparison with State-of-the-art Methods

We evaluate our method against state-of-the-art patch-distributing and pixel-distributing approaches, including ClassSR [12], ARM [3], and PCSR [9], which represent the most relevant baselines for adaptive computation allocation. Following [3, 9, 12], we use PSNR to assess the quality of the SR images and FLOPs to measure the efficiency. Notably, we exclude quantization and knowledge distillation methods from our comparisons, as these acceleration techniques can be seamlessly integrated with our framework to achieve acceleration without conflict. As evidenced by the quantitative analysis in Table 2, our approach achieves competitive reconstruction quality without introducing additional parameters or computation. Concurrently, we have observed that there is a correlation between the network performance and the computation proportion of the body part network. It explains the varying efficacy of our method across architectures, providing moderate FLOPs reduction (15%) in extremely lightweight architectures like FSRCNN, but it achieves significant computational savings (almost 42%) in deeper architectures such as SwinIR and CARN. Moreover, crucially, our method demonstrates a substantial advantage in actual runtime compared to other acceleration methods, as detailed in Table 3.

We also provide qualitative results with the PSNR and FLOPs of each SR result for better comparisons in Fig. 3. Patch-distributing methods such as ClassSR and ARM are incapable of performing fine-grained segmentation of regions. In contrast, our method can more precisely process different regions of the input image, thereby achieving efficient and effective image super-resolution with comparable results at a lower computation. Comparing to PCSR, which applies processing with varying levels of complexity to different regions only in the tail part of the network and shows significant benefits only for very small networks, such as

FSRCNN, our method is applied to the main body of the networks, which can result in greater savings of computation for the vast majority of networks, particularly those high-performance networks. Furthermore, the compatibility of our method with Transformer-based architectures is noteworthy. It can be seamlessly integrated with minimal adjustments, ensuring a significant decrease in FLOPs without compromising performance as shown in Fig. 4.

4.3. Generalization to Unseen Degradations

Due to the occurrence of more complex degradations in real-world SR scenarios, to verify the robustness of our high-frequency mask against complex degradations, we employed a random degradation pipeline [32] that includes other unseen degradations during the training process, such as noise and compression. Fig. 5 illustrates the impact of unseen degradations on different SR acceleration methods. Through the fluctuation of computation and visual comparison of masks, our method exhibits exceptional resilience to unseen degradations encountered during inference. ARM demonstrates pronounced sensitivity to degradation-domain shifts, leading it to classify most patches as hard regions (red areas), which greatly increases the computation. Both ClassSR and PCSR are affected to some extent. For instance, noises in the sky can influence the classification results of PCSR. Furthermore, considering the degradation gap between training and testing, the results of all methods exhibit some artifacts. However, our method still demonstrates superior quantitative metrics.

4.4. Ablation Study

4.4.1. Mask Generation

We analyze the impact of different strategies for generating high-frequency masks, investigating the following variants: 1) normalize the high-frequency map and compare it with a fixed threshold value of 0.5, 2) compare the high-frequency

Threshold σ	Test2K		Test4K		Test8K	
	PSNR	GFLOPs	PSNR	GFLOPs	PSNR	GFLOPs
1.0	25.264	15.5 (15.1%)	26.469	61.3 (14.8%)	32.267	350.6 (14.6%)
0.7	26.218	66.0 (64.3%)	27.640	237.8 (57.3%)	33.513	1097.3 (45.7%)
0.5	26.299	70.6 (68.8%)	27.746	256.8 (61.9%)	33.611	1207.6 (50.3%)
0.3	26.331	73.9 (72.0%)	27.787	270.8 (65.3%)	33.645	1293.1 (53.9%)
0.0	26.356	102.6 (100%)	27.828	415.0 (100%)	33.686	2399.8 (100%)

Table 5. The impact of pruning threshold on SwinIR.

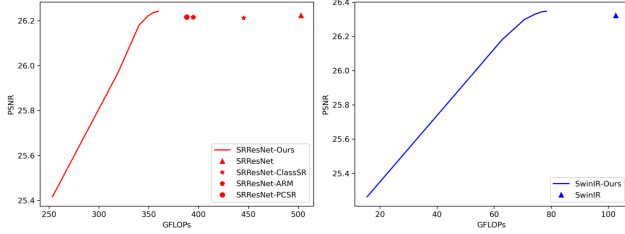


Figure 6. The impact of dilation kernels with different sizes on various backbones. Expanding the kernel size will enhance the performance, yet unavoidably induce increasing computation, thereby establishing an inherent trade-off.

map with its median value, 3) utilize K-means clustering to adaptively generate a binary mask focus on high-frequency regions, and apply a dilation operation with a kernel size of 3 to the mask to ensure a comparable computation for a fair comparison. We take CARN as an example and the results are shown in Table 4. As demonstrated, the adaptive selection strategy is more capable of adjusting the mask according to each image, achieving superior performance with a comparable computation compared to other strategies.

4.4.2. Dilation Kernel

Our method demonstrates exceptional computation scalability through dilation-based mask adaptation, eliminating the need for retraining. As depicted in Fig. 6, we analyze the effects of varying kernel sizes in the dilation operation, from 1 to 11, on the performance and computation of both the CNN-based method SRResNet and the Transformer-based method SwinIR. It can be observed that due to the body part of SwinIR constituting a significantly larger proportion (99%) of the overall computation compared to that in SRResNet (47%), making its computation more sensitive to kernel size adjustments. Despite these differences, our method consistently attains results on par with other methods, while incurring a significantly lower computation – 30.5% and 31% computational savings for SRResNet and SwinIR respectively.

4.4.3. Pruning Threshold

Unlike CNN-based approaches, Transformer-based methods process tokens generated through non-overlapping window partitioning. This architectural distinction introduces

two critical hyperparameters governing computational efficiency: the size of the dilation kernel and the pruning threshold σ . Through systematic analysis with a fixed kernel size (set to 5), we evaluate threshold sensitivity across performance and efficiency. As quantitatively demonstrated in Table 5, $\sigma = 0.5$ achieves 31-50% FLOPs reduction while maintaining reconstruction quality ($\Delta\text{PSNR} < 0.16$ dB) across benchmark datasets.

5. Limitations and Future Work

Despite our method achieving comparable performance with lower computation and inference time, its optimization scope is primarily confined to the body part of the SR network. This approach exhibits inconsistent acceleration across diverse network architectures, particularly in shallow models like FSRCNN. The computation within the body part is extremely small, thereby imposing fundamental limitations on the theoretical maximum acceleration attainable through architectural optimization strategies. Subsequently, we plan to integrate existing methods that specifically target the tail part of the SR network while ensuring minimal introduction of artifacts, to further refine and enhance our approach.

6. Conclusion

In this paper, we propose a straightforward and effective strategy to accelerate SISR methods. We leverage training-free operations to obtain high-frequency maps and employ K-means clustering to generate a pruning mask, which is then applied to the body part of the SR method, which ensures that the network focuses on processing only the more challenging regions for the SR task, thereby reducing computation. Our strategy is effective for both CNN-based and Transformer-based methods, and we can control the amount of pixels/tokens that require processing during the inference by applying dilation operations to the mask, achieving satisfactory scalability. Experiments demonstrate that our acceleration strategy is robust under unseen degradations and achieves comparable results to other methods with less computation. In the future, we plan to extend our strategy further to video SR methods to achieve acceleration.

References

- [1] Eirikur Agustsson and Radu Timofte. Ntire 2017 challenge on single image super-resolution: Dataset and study. In *Proceedings of the IEEE/CVF Conference on Computer Vision and Pattern Recognition Workshops*, pages 126–135, 2017.
- [2] Namhyuk Ahn, Byungkun Kang, and Kyung-Ah Sohn. Fast, accurate, and lightweight super-resolution with cascading residual network. In *European Conference on Computer Vision*, pages 252–268, 2018.
- [3] Bohong Chen, Mingbao Lin, Kekai Sheng, Mengdan Zhang, Peixian Chen, Ke Li, Liujuan Cao, and Rongrong Ji. ARM: Any-time super-resolution method. In *European Conference on Computer Vision*, pages 254–270, 2022.
- [4] Hanting Chen, Yunhe Wang, Tianyu Guo, Chang Xu, Yiping Deng, Zhenhua Liu, Siwei Ma, Chunjing Xu, Chao Xu, and Wen Gao. Pre-trained image processing Transformer. In *Proceedings of the IEEE/CVF Conference on Computer Vision and Pattern Recognition*, pages 12299–12310, 2021.
- [5] Xiangyu Chen, Xintao Wang, Jiantao Zhou, Yu Qiao, and Chao Dong. Activating more pixels in image super-resolution Transformer. In *Proceedings of the IEEE/CVF Conference on Computer Vision and Pattern Recognition*, pages 22367–22377, 2023.
- [6] Chao Dong, Chen Change Loy, Kaiming He, and Xiaoou Tang. Learning a deep convolutional network for image super-resolution. In *European Conference on Computer Vision*, pages 184–199, 2014.
- [7] Chao Dong, Chen Change Loy, and Xiaoou Tang. Accelerating the super-resolution convolutional neural network. In *European Conference on Computer Vision*, pages 391–407, 2016.
- [8] Shuhang Gu, Andreas Lugmayr, Martin Danelljan, Manuel Fritsche, Julien Lamour, and Radu Timofte. DIV8K: Diverse 8K resolution image dataset. In *Proceedings of the IEEE/CVF International Conference on Computer Vision Workshop*, pages 3512–3516, 2019.
- [9] Jinho Jeong, Jinwoo Kim, Younghyun Jo, and Seon Joo Kim. Accelerating image super-resolution networks with pixel-level classification. In *European Conference on Computer Vision*, pages 236–251, 2024.
- [10] Jiwon Kim, Jung Kwon Lee, and Kyoung Mu Lee. Accurate image super-resolution using very deep convolutional networks. In *Proceedings of the IEEE/CVF Conference on Computer Vision and Pattern Recognition*, pages 1646–1654, 2016.
- [11] Diederik P Kingma and Jimmy Ba. Adam: A method for stochastic optimization. In *International Conference on Learning Representations*, 2014.
- [12] Xiangtao Kong, Hengyuan Zhao, Yu Qiao, and Chao Dong. ClassSR: A general framework to accelerate super-resolution networks by data characteristic. In *Proceedings of the IEEE/CVF Conference on Computer Vision and Pattern Recognition*, pages 12016–12025, 2021.
- [13] Christian Ledig, Lucas Theis, Ferenc Huszár, Jose Caballero, Andrew Cunningham, Alejandro Acosta, Andrew Aitken, Alykhan Tejani, Johannes Totz, Zehan Wang, et al. Photo-realistic single image super-resolution using a generative adversarial network. In *Proceedings of the IEEE/CVF Conference on Computer Vision and Pattern Recognition*, pages 4681–4690, 2017.
- [14] Royson Lee, Łukasz Dudziak, Mohamed Abdelfattah, Stylianos I Venieris, Hyeji Kim, Hongkai Wen, and Nicholas D Lane. Journey towards tiny perceptual super-resolution. In *European Conference on Computer Vision*, pages 85–102, 2020.
- [15] Wonkyung Lee, Junghyup Lee, Dohyung Kim, and Bumsuh Ham. Learning with privileged information for efficient image super-resolution. In *European Conference on Computer Vision*, pages 465–482, 2020.
- [16] Huixia Li, Chenqian Yan, Shaohui Lin, Xiawu Zheng, Baoshang Zhang, Fan Yang, and Rongrong Ji. Pams: Quantized super-resolution via parameterized max scale. In *European Conference on Computer Vision*, pages 564–580, 2020.
- [17] Zheyuan Li, Yingqi Liu, Xiangyu Chen, Haoming Cai, Jinjin Gu, Yu Qiao, and Chao Dong. Blueprint separable residual network for efficient image super-resolution. In *Proceedings of the IEEE/CVF Conference on Computer Vision and Pattern Recognition*, pages 833–843, 2022.
- [18] Jingyun Liang, Jiezhang Cao, Guolei Sun, Kai Zhang, Luc Van Gool, and Radu Timofte. SwinIR: Image restoration using swin Transformer. In *Proceedings of the IEEE/CVF International Conference on Computer Vision Workshops*, pages 1833–1844, 2021.
- [19] Bee Lim, Sanghyun Son, Heewon Kim, Seungjun Nah, and Kyoung Mu Lee. Enhanced deep residual networks for single image super-resolution. In *Proceedings of the IEEE/CVF Conference on Computer Vision and Pattern Recognition Workshops*, pages 136–144, 2017.
- [20] Kai Liu, Haotong Qin, Yong Guo, Xin Yuan, Linghe Kong*, Guihai Chen, and Yulun Zhang. 2DQuant: Low-bit post-training quantization for image super-resolution. In *Conference on Neural Information Processing Systems*, 2024.
- [21] Ming Liu, Zhilu Zhang, Liya Hou, Wangmeng Zuo, and Lei Zhang. Deep adaptive inference networks for single image super-resolution. In *European Conference on Computer Vision Workshops*, pages 131–148, 2020.
- [22] Ilya Loshchilov and Frank Hutter. SGDR: Stochastic gradient descent with warm restarts. In *International Conference on Learning Representations*, 2017.
- [23] Sung Cheol Park, Min Kyu Park, and Moon Gi Kang. Super-resolution image reconstruction: a technical overview. *IEEE Signal Processing Magazine*, 20(3):21–36, 2003.
- [24] Wenzhe Shi, Jose Caballero, Christian Ledig, Xiaohai Zhuang, Wenjia Bai, Kanwal Bhatia, Antonio M Simoes Monteiro de Marvao, Tim Dawes, Declan O’Regan, and Daniel Rueckert. Cardiac image super-resolution with global correspondence using multi-atlas patchmatch. In *Medical Image Computing and Computer-Assisted Intervention*, pages 9–16, 2013.
- [25] Longguang Wang, Xiaoyu Dong, Yingqian Wang, Xinyi Ying, Zaiping Lin, Wei An, and Yulan Guo. Exploring sparsity in image super-resolution for efficient inference. In *Proceedings of the IEEE/CVF Conference on Computer Vision and Pattern Recognition*, pages 4917–4926, 2021.

- [26] Shizun Wang, Jiaming Liu, Kaixin Chen, Xiaoqi Li, Ming Lu, and Yandong Guo. Adaptive patch exiting for scalable single image super-resolution. In *European Conference on Computer Vision*, pages 292–307, 2022.
- [27] Zhou Wang, Alan C Bovik, Hamid R Sheikh, and Eero P Simoncelli. Image quality assessment: From error visibility to structural similarity. *IEEE Transactions on Image Processing*, 13(4):600–612, 2004.
- [28] Wenbin Xie, Dehua Song, Chang Xu, Chunjing Xu, Hui Zhang, and Yunhe Wang. Learning frequency-aware dynamic network for efficient super-resolution. In *Proceedings of the IEEE/CVF International Conference on Computer Vision*, pages 4308–4317, 2021.
- [29] Jingwei Xin, Nannan Wang, Xinrui Jiang, Jie Li, Heng Huang, and Xinbo Gao. Binarized neural network for single image super resolution. In *European Conference on Computer Vision*, pages 91–107, 2020.
- [30] Eduard Zamfir, Marcos V Conde, and Radu Timofte. Towards real-time 4K image super-resolution. In *Proceedings of the IEEE/CVF Conference on Computer Vision and Pattern Recognition Workshops*, pages 1522–1532, 2023.
- [31] Zheng Zhan, Yifan Gong, Pu Zhao, Geng Yuan, Wei Niu, Yushu Wu, Tianyun Zhang, Malith Jayaweera, David Kaeli, Bin Ren, et al. Achieving on-mobile real-time super-resolution with neural architecture and pruning search. In *Proceedings of the IEEE/CVF International Conference on Computer Vision*, pages 4821–4831, 2021.
- [32] Kai Zhang, Jingyun Liang, Luc Van Gool, and Radu Timofte. Designing a practical degradation model for deep blind image super-resolution. In *Proceedings of the IEEE/CVF International Conference on Computer Vision*, pages 4791–4800, 2021.
- [33] Yulun Zhang, Kunpeng Li, Kai Li, Lichen Wang, Bineng Zhong, and Yun Fu. Image super-resolution using very deep residual channel attention networks. In *European Conference on Computer Vision*, pages 286–301, 2018.
- [34] Yulun Zhang, Yapeng Tian, Yu Kong, Bineng Zhong, and Yun Fu. Residual dense network for image super-resolution. In *Proceedings of the IEEE/CVF Conference on Computer Vision and Pattern Recognition*, pages 2472–2481, 2018.
- [35] Yiman Zhang, Hanting Chen, Xinghao Chen, Yiping Deng, Chunjing Xu, and Yunhe Wang. Data-free knowledge distillation for image super-resolution. In *Proceedings of the IEEE/CVF Conference on Computer Vision and Pattern Recognition*, pages 7852–7861, 2021.
- [36] Hengyuan Zhao, Xiangtao Kong, Jingwen He, Yu Qiao, and Chao Dong. Efficient image super-resolution using pixel attention. In *European Conference on Computer Vision Workshops*, pages 56–72, 2020.
- [37] Wilman WW Zou and Pong C Yuen. Very low resolution face recognition problem. *IEEE Transactions on Image Processing*, 21(1):327–340, 2011.